RSC Advances

PAPER

View Article Online
View Journal | View Issue

Cite this: *RSC Adv.*, 2026, **16**, 9578

DFT study of halogenated InTeX (X = Cl, Br and I) monolayers: promising 2D materials for nanoelectronics

Tuan V. Vu, †*[ab] Dat D. Vo,[c] Oleg Khyzhun,[cd] Michał Piasecki,[c] Thi H. Ho[ab] and Nguyen N. Hieu[ef]

First-principles calculations were performed to investigate the structural, electronic, mechanical, and spintronic properties of InTeX (X = Cl, Br, and I) monolayers formed *via* full halogenation of pristine InTe. Halogenation induces a structural transformation from the four-sublayer Te–In–In–Te configuration to a three-sublayer Te–In–X geometry, accompanied by the formation of polar covalent In–X bonds and the suppression of metallic In–In interactions. The resulting monolayers preserve a buckled hexagonal lattice and exhibit enhanced thermodynamic, thermal, and dynamical stability. InTeX monolayers display moderate Young's moduli (22.18–25.26 N m^{-1}), isotropic in-plane elastic behavior, and Poisson's ratios from 0.31 to 0.32, rendering them promising candidates for flexible and wearable nanoelectronic applications. The electronic band structures reveal tunable direct band gaps and strong, anisotropic Rashba spin–orbit coupling, with Rashba parameters α_R ranging from 0.81 to 1.04 eV Å, indicating potential for spintronic and optospintronic devices. Importantly, charge-carrier mobilities were evaluated by explicitly accounting for phonon and impurity scattering, yielding realistic values consistent with experimental expectations and underscoring the importance of accurate mobility modeling for device performance. Overall, the combination of structural stability, tunable electronic properties, robust spin–orbit effects, and reliable carrier transport makes InTeX monolayers highly promising materials for future research in flexible electronics, spintronics, and multifunctional two-dimensional nanomaterials.

Received 8th January 2026
Accepted 11th February 2026

DOI: 10.1039/d6ra00185h

rsc.li/rsc-advances

1 Introduction

Group-III monochalcogenide monolayers (MX, where M = Ga, In and X = S, Se, and Te) occupy a unique and important position in the field of two-dimensional (2D) materials.[1] These monolayers exhibit a wide range of band gaps, spanning from 0.78 to 4.43 eV,[2] which makes them suitable for applications in nanoelectronics, photocatalysis, and photovoltaics. Notably, few-layer InSe has been reported to exhibit ultrahigh carrier mobility at room temperature (up to 10^3–10^4 cm^2 V^{-1} s^{-1}), together with remarkable elastic deformability.[3] These monolayers can be formed by combining a wide variety of two or three elements, leading to significant diversity in both their crystal structures and physical properties. For instance, fluorinated InSe (InSeF) exhibits pronounced in-plane elastic anisotropy.[4] In addition, InX monolayers (X = O, S, Se, and Te) are predicted to be mechanically isotropic in terms of Young's modulus and Poisson's ratio, with InO showing the highest calculated stiffness of 79.1 N m^{-1}.[5] These mechanical characteristics render such materials promising candidates for ultraviolet-selective photodetectors, water splitting, and other optoelectronic applications.[6,7]

In recent years, surface functionalization has emerged as an effective and widely adopted approach for tailoring the physical properties of two-dimensional materials. For example, oxygen functionalization of InS, InSe, and InTe can modulate electronic properties, producing 2D topological insulators with substantial bulk gaps of up to 0.21 eV.[8] Hydrogenation similarly induces phase-dependent behavior in GaSe, where single-sided H-GaSe is metallic, whereas double-sided 2H-GaSe remains a semiconducting material.[9] In addition, surface hydrogenation leads to a transition from an indirect to a direct band-gap semiconductor in AlN.[10] Halogenation strategies further expand the chemical space, generating compounds such as GaXY (X = S, Se; Y=F, Cl, Br, I) with enhanced piezoelectric responses.[2] Additional approaches include strain and electric-field engineering

[a]*Laboratory for Computational Physics, Institute for Computational Science and Artificial Intelligence, Van Lang University, Ho Chi Minh City, Vietnam. E-mail: tuan.vu@vlu.edu.vn*

[b]*Faculty of Mechanical, Electrical, and Computer Engineering, Van Lang School of Technology, Van Lang University, Ho Chi Minh City, Vietnam*

[c]*Faculty of Science and Technology, Jan Długosz University, Armii Krajowej 13/15, Czestochowa, PL-42200, Poland*

[d]*Frantsevich Institute for Problems of Materials Science, National Academy of Sciences of Ukraine, 3 Omeljan Pritsak Str., Kyiv, UA-03142, Ukraine*

[e]*Institute of Research and Development, Duy Tan University, Da Nang 550000, Vietnam*

[f]*Faculty of Natural Sciences, Duy Tan University, Da Nang 550000, Vietnam*

† To whom correspondence should be addressed.

to induce indirect-to-direct band gap transitions or semiconductor-to-metal phase changes,[11] as well as transition-metal doping or vacancy/hole engineering in InTe to introduce magnetic properties.[11]

Among group-III monochalcogenides, InTe monolayers are particularly notable for their relatively narrow indirect band gaps,[12] which allow them to be at the interface of visible and near-infrared absorption. The InTe monolayer demonstrates high dynamical stability, as confirmed by phonon spectrum analysis,[13] and exhibits isotropic in-plane stiffness. The InTe monolayer is also suitable for diverse and precisely tunable modification strategies. Transition-metal doping (TM = Ti, V, Cr, Mn, Fe, Co), when combined with strain engineering, can induce magnetism and half-metallicity, with Cr-doped systems achieving Curie temperatures up to 265 K.[14] Vacancy defects and hole doping further enable tunable magnetic and electronic properties[11] of a InTe monolayer. Surface functionalization *via* fluorination (InTeF) transforms the InTe monolayer into a direct-gap semiconductor with a 2.48 eV energy gap and a significant Rashba spin splitting (α_R of about 1.08 eV Å).[15] Related halogenated compounds, such as InTeI, are predicted to exhibit wide band gaps and highly anisotropic carrier mobilities.[16] Strain and electric-field modulation can further tune the band structure and induce semiconductor-to-metal transitions,[11] highlighting the diversity in potential applications of InTe-based materials.[17]

Although fluorination of InTe has been extensively investigated,[15] non-fluorine halogen functionalization (InTe–Cl, InTe–Br, and InTe–I) remains largely unexplored, despite analogous GaXY (Y = Cl, Br, I) compounds having been successfully predicted.[2] wing to the larger atomic masses and stronger spin–orbit coupling of Cl, Br, and especially I, halogen functionalization in a Janus configuration is expected to significantly enhance Rashba spin splitting. This enhancement originates from the intrinsic out-of-plane inversion-symmetry breaking introduced by the Janus structure, which generates a built-in electric field. The Rashba effect induced by this Janus asymmetry can be further strengthened by incorporating large-sized halogen elements, thereby enabling tunable direct band gaps and offering additional flexibility for electronic property engineering. Moreover, the symmetry breaking in Janus structures can also give rise to a variety of intriguing topological properties.[18–20] Therefore, in this study the structural and electronic properties of InTeX (X = Cl, Br and I) monolayers are studied using first-principles calculations. It is worth nothing that there is a large difference in the values of charge carrier mobility of a InTe monolayer when it was calculated with and without the inclusion of scattering effects.[16,21] Therefore, the transport properties of InTeX (X = Cl, Br and I) monolayers are investigated with the inclusion of four scattering mechanisms. Moreover, the dependence of transport properties on the temperature and carrier concentration is also analyzed.

2 Computational details

Density functional theory calculations were conducted using VASP, with core–valence interactions described by the projector-augmented wave (PAW) method[22,23] and exchange–correlation effects treated within the Perdew–Burke–Ernzerhof (PBE) functional.[24] InTeX (X = Cl, Br, and I) monolayers were constructed from the buckled InTe structure[16] and optimized using a 25 Å vacuum layer to eliminate artificial periodic interactions.[25] Because indium, tellurium, and the heavier halogen atoms introduce non-negligible relativistic effects, selected calculations included spin–orbit coupling to evaluate its impact on the electronic band structure. Long-range dispersion interactions were incorporated during structural optimization using the DFT-D3 correction suggested by Grimme.[26] The electronic band structures and band gaps were further refined using the screened hybrid HSE06 functional with 25% exact exchange.[27] Brillouin zone integration was performed on a 15 × 15 × 1 Monkhorst–Pack grid,[28] while a plane-wave cutoff energy of 500 eV was used. Self-consistent electronic calculations were converged to within 1×10^{-5} eV, and structural optimization proceeded until atomic forces were less than 1×10^{-4} eV Å^{-1}. Additional test calculations using a tighter threshold of 1×10^{-8} eV resulted in negligible changes to the total energies and key physical properties, confirming the reliability of the adopted convergence settings. Dynamical stability was assessed by phonon calculations based on second-order force constants obtained *via* the finite-displacement technique, as implemented in the PHONOPY code, using a 4 × 4 × 1 supercell.[29]

Charge-transport parameters were extracted from density functional theory and density functional perturbation theory (DFT/DFPT) calculations.[29,30] Mode-resolved electron–phonon and impurity coupling matrix elements were evaluated and interpolated to determine scattering rates associated with acoustic deformation-potential (ADP), polar optical-phonon (POP), ionized impurity (IMP), and piezoelectric (PIE) mechanisms using the AMSET framework.[31] These scattering processes were treated within the relaxation-time approximation of the Boltzmann transport equation and combined according to Matthiessen's rule to obtain the total carrier mobilities.[32]

3 Calculated results and discussion

3.1 Structural characteristics of InTeX (X = Cl, Br, I) monolayers

In agreement with previous studies, the optimized pristine InTe monolayer was found to adopt a hexagonal crystal structure with space group *P6m2*, consisting of four atoms in the primitive cell. The calculated lattice constant is 4.35 Å, with an In–Te bond length of 2.87 Å and a thickness of 5.56 Å. These values are very close to those reported in earlier studies, differing only slightly by 0.02–0.04 Å.[13,33,34] As shown in Fig. 1(a), the fully halogenated InTe monolayers preserve the hexagonal arrangement in the top view. However, the side view in Fig. 1(b) reveals a pronounced structural transformation. Instead of the four-sublayer sequence (Te–In–In–Te) observed in pristine InTe, the halogenated structures InTeX (X = Cl, Br, I) consist of only three sublayers arranged in the order Te–In–X. This structural modification arises from changes in the electronic structure, which will be discussed in detail in the following sections.

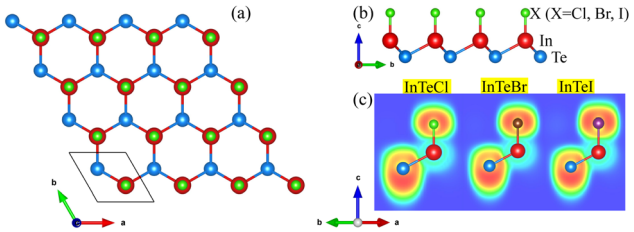

Fig. 1 (a) Side view, (b) another side view and (c) electron localization functions (ELF) of InTeX (X = Cl, Br, I) monolayers.

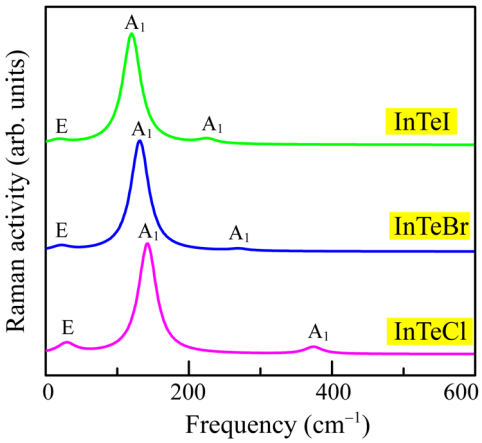

Fig. 2 Calculated Raman spectra of InTeX (X = Cl, Br, I) monolayers.

The electron localization function (ELF), presented in Fig. 1(c), provides an initial insight into the bonding characteristics of the new monolayers. The regions between In or Te and the halogen atoms (Cl, Br, I) are highlighted in cyan-green, indicating a high density of shared electrons consistent with covalent bonding in In–X and Te–X. A notable feature is the significant asymmetric charge distribution in all three monolayers, remarkably highlighted by strong red regions around the halogen and Te atoms, corresponding to charge-attracting sites. In contrast, the cyan regions around the In atoms reflect low charge density, implying that the In–Te and In–X bonds can be regarded as distinct dipoles. These dipoles are oriented in different directions, leading to a net nonzero dipole moment in the halogenated monolayers. This redistribution of charge induces subtle structural variations in the halogenated InTe monolayers compared to the pristine layer. As summarized in Table 1, the In–Te bond lengths remain nearly unchanged, whereas the 2D unit cells of InTeCl, InTeBr, and InTeI expand due to an increase in the lattice parameter *a*. This expansion can be attributed to enhanced Coulomb repulsion between Te atoms, which become more negatively charged upon halogenation. For instance, the calculated Bader charge on Te atoms in the InTeI monolayer is 0.12*e*, making them the most negatively charged centers among the three halogenated systems, and consequently leading to the largest unit-cell expansion.

The pristine InTe monolayer exhibits a thickness of 5.56 Å, which is significantly reduced in the halogenated monolayers due to the transition from a four-sublayer (Te–In–In–Te) to a three-sublayer (Te–In–X) configuration. In addition, the In–X bond length plays a crucial role: halogens with lower electronegativity (I < Br < Cl) form longer bonds with In, resulting in thicker monolayers as the halogen size increases. A similar trend has been reported in halogenated SnS monolayers, where the Sn–X bond length increases with halogen atomic size (F < Cl < Br < I). Accordingly, the attachment of heavier halogens leads to a slight increase in the effective thickness of the halogenated InTe monolayers.[35] Halogen atoms with very high electronegativity, such as F, can induce structural instabilities, as observed in GaSF and GaSeF monolayers,[2] or even drive a phase transition, as in the case of InSeF.[4] The phase change in the InSeF monolayer can be rationalized by considering the behavior of InTeX (X = Cl, Br, I) systems: the excessive charge transfer to the highly electronegative F atom significantly reduces the charge density on In atoms, thereby weakening their ability to stabilize the in-plane hexagonal framework.

The calculated Raman spectra of the halogenated InTeX (X = Cl, Br, I) monolayers, as shown in Fig. 2, display a characteristic three-peak pattern that distinguishes them from both pristine InSe and InSeF monolayers reported in previous studies.[4,36,37] Each InTeX compound exhibits exactly three Raman-active modes with one degenerate E mode (in-plane) at low frequency and two A_1 modes (out-of-plane), which is fully consistent with the reduced symmetry of the three-sublayer structures. With increasing halogen mass when going from Cl to Br and, then, to I, all Raman-active modes exhibit a clear and systematic red-shift. The E mode softens from around 40 cm^{-1} to about 20 cm^{-1}, while the lower A_1 mode decreases from 145 cm^{-1} to nearly 120 cm^{-1}. The higher A_1 mode undergoes the most pronounced shift, dropping from approximately 380 cm^{-1} to around 230 cm^{-1}. Throughout the series, the intensity distribution remains nearly identical, where the lower A_1 mode dominates the spectrum by a large margin, followed by the E mode, whereas the higher A_1 mode is consistently weak. This dominant lower A_1 peak therefore serves as a clear spectroscopic marker of successful halogenation. Compared to the InSe monolayer with four-sublayer structure, which typically

Table 1 Structural, energetic and mechanical properties of InTeX (X = Cl, Br and I) monolayers and related parameters: lattice constant *a* (Å), bond length *d* (Å), and monolayer's thickness *h* (Å); cohesive energy E_c (eV); elastic constants C_{11}, C_{12}, C_{66}, and Young's modulus Y (N m^{-1}); and Poisson's ratio ν; piezoelectric parameters e_{11} and e_{31} (10^{-10} Cm^{-1}), d_{11} and d_{31} (pmV^{-1})

	a	d_{In-Te}	d_{In-X}	h	E_f	C_{11}	C_{12}	C_{66}	Y	ν	e_{11}	e_{31}	d_{11}	d_{31}
InTeCl	4.38	2.86	2.32	3.66	−3.41	24.65	7.81	8.43	22.18	0.32	−1.87	−0.33	−11.08	−1.01
InTeBr	4.37	2.86	2.46	3.81	−2.99	25.55	7.99	8.78	23.05	0.31	−1.55	−0.23	−8.81	−0.68
InTeI	4.40	2.87	2.66	4.00	−2.55	27.90	8.53	9.61	25.26	0.31	−1.31	−0.12	−6.75	−0.34

shows four to five strong features, the InTeX family presents a much simpler spectrum with significantly lower frequencies, wider mode separation, and no overlap between E and A_1 branches, the effects that arise from the heavier Te atoms, elimination of the In–In dimer, and overall lattice softening. These pronounced, mass-dependent shifts and the minimal three-peak profile offer a straightforward and reliable way to identify and differentiate InTeCl, InTeBr, and InTeI monolayers experimentally, with InTeI exhibiting the lowest-frequency and most widely spaced triplet and InTeCl the highest-frequency and most compact one.

The stability of InTeX (X = Cl, Br, I) monolayers was first evaluated through their cohesive energy, E_c, defined as $E_f = E_{InTeX} - E_{InTe} - E_X$, where E_{InTeX}, E_{InTe}, and E_X represent the total energies of the halogenated InTeX monolayer, the pristine InTe monolayer, and an isolated halogen atom, respectively. As summarized in Table 1, the calculated formation energies of all three halogenated monolayers are noticeably negative, ranging from −3.41 to −2.55 eV, indicating that they are thermodynamically more stable than the isolated InTe monolayer and halogen atoms. Thermal stability was further assessed *via ab initio* molecular dynamics (AIMD) simulations at 300 K for 5 ps. As shown in Fig. 3(b), the total energy of each system fluctuates around well-defined equilibrium values without any abrupt or significant changes. These results demonstrate that the halogenated InTeX monolayers remain thermally stable under room-temperature conditions.

With the growing interest in two-dimensional (2D) materials for applications in electronics, energy storage, and flexible devices,[38–40] evaluating their dynamic stability is essential for reliable performance under practical conditions. For pristine InTe and halogenated InTeX (X = Cl, Br, I) monolayers, phonon dispersion spectra provide direct insight into their stability, as shown in Fig. 3(a). All four systems display smooth, positive phonon branches, confirming dynamical stability. The pristine InTe monolayer exhibits moderate curvature in both acoustic and optical phonon modes, reflecting strong vibrational coupling and relatively stiff atomic bonding. Halogenation, however, induces a downward shift and flattening of the acoustic branches, most pronounced in InTeCl due to the lighter mass of Cl. This trend indicates reduced lattice stiffness, consistent with the decrease in Young's modulus values (Table 1): 25.26 N m^{-1} for InTeI, 23.05 N m^{-1} for InTeBr, and 22.18 N m^{-1} for InTeCl. Halogen substitution also alters the separation between acoustic and optical branches. Among the halogenated monolayers, InTeBr exhibits the widest phonon band gap, suggesting suppressed optical phonon scattering of charge carriers and implying superior carrier mobility relative to the other systems.

To further investigate the mechanical properties of InTeX (X = Cl, Br, I) monolayers, their elastic constants were calculated and are summarized in Table 1. For 2D hexagonal crystals, the independent non-zero elastic constants are C_{11}, C_{12}, C_{66},[41] which can be obtained from the unit cell area (Ω) and the strain–energy function E_ε through the relation $C_{ij} = \Omega^{-1}\partial^2 E_\varepsilon / \partial\varepsilon_i\partial\varepsilon_j$. The Young's modulus ($Y$) and Poisson's ratio ($\nu$) are then derived from these elastic constants as $Y = (C_{11}^2 - C_{12}^2)/C_{11}$ and $\nu = C_{12}/C_{11}$. According to Born's mechanical stability criteria for 2D hexagonal structures,[42] the InTeX monolayers satisfy the conditions $C_{11} > 0$ and $C_{11} > C_{12}$, confirming their mechanical stability. The calculated Young's moduli of the three halogenated monolayers fall within the range of 22.18–25.26 N m^{-1}, closely matching those of stanene, black phosphorene, tin sulfide, and chromium triiodide, all of which have already been established as highly promising materials for flexible electronics, nano-transistors, piezoelectric devices, and ferroelectric systems.[43–45] Therefore, the comparable elastic properties of InTeX monolayers highlight their potential as promising candidates for diverse applications. In addition, their Poisson's ratios, lying between 0.31 and 0.32, represent another advantageous feature. Monolayers with similar Poisson's ratios – such as MoS_2, GaS, GaSe, hexagonal $MoTe_2$, $MoSi_2N_4$, and $Ti_3C_2O_2$ have already been demonstrated as suitable for coatings, wearable devices, and other flexible applications,.[46,47]

Mechanical isotropy is a crucial requirement for 2D materials, as it prevents anisotropic failure and ensures reliable performance in flexible or wearable devices regardless of bending or stretching direction. To examine this property in InTeX (X = Cl, Br, I) monolayers, the angular dependence of Young's modulus $Y(\alpha)$ and Poisson's ratio $\nu(\alpha)$ was analyzed, with their directional variation expressed by the following relations:[48,49]

$$Y(\alpha) = \frac{C_{11}C_{22} - C_{12}^2}{C_{11}\sin^4\alpha + C_{22}\cos^4\alpha + \left(\frac{C_{11}C_{22} - C_{12}^2}{C_{66}} - 2C_{12}\right)\sin^2\alpha\cos^2\alpha} \quad (1)$$

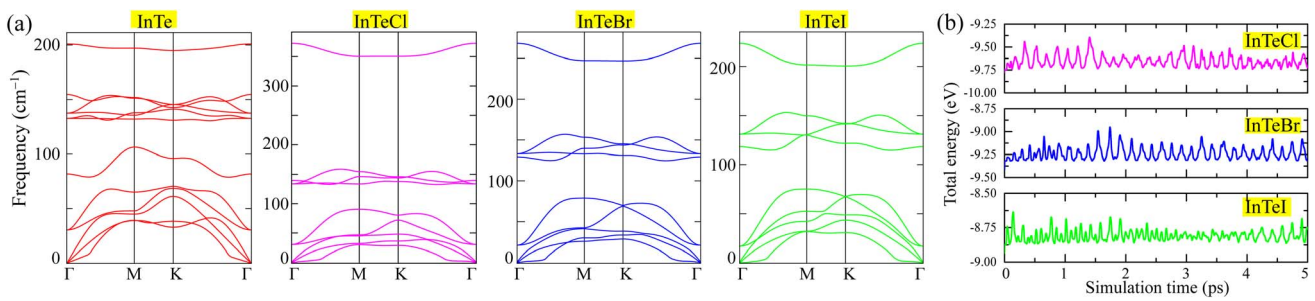

Fig. 3 (a) Phonon dispersion and (b) time-dependence energy of pristine InTe and InTeX (X = Cl, Br, and I) monolayers.

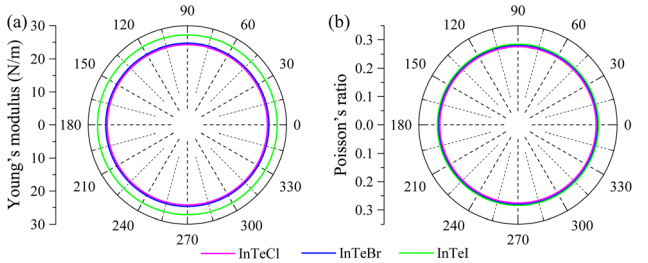

Fig. 4 (a) Polar diagrams of Young's modulus and (b) Poisson's ratio of InTeX (X = Cl, Br, I) monolayers.

$$\upsilon(\alpha) = \frac{C_{12}\left(\sin^4\alpha + \cos^4\alpha\right) - \left(C_{11} + C_{22} - \dfrac{C_{11}C_{22} - {C_{12}}^2}{C_{66}}\right)\sin^2\alpha\cos^2\alpha}{C_{11}\sin^4\alpha + C_{22}\cos^4\alpha - \left(2C_{12} - \dfrac{C_{11}C_{22} - {C_{12}}^2}{C_{66}}\right)\sin^2\alpha\cos^2\alpha} \quad (2)$$

As shown in Fig. 4, the values of $Y(\alpha)$ and $\nu(\alpha)$ remain nearly constant over all in-plane angles α. Similar to the pristine InTe monolayer,[5] the mechanical properties of halogenated InTeX (X = Cl, Br, I) monolayers are almost independent of strain direction, confirming their elastic isotropy. Generally, the combination of moderate stiffness, isotropic elasticity, and well-balanced Poisson's ratio makes the halogenated InTeX monolayers highly attractive for flexible nanoelectronic devices, high-sensitivity sensors, and conformal coatings-applications that demand ultrathin materials to be simultaneously robust and mechanically compliant.[50–52]

The InTeX (X = Cl, Br and I) monolayers exhibit significant intrinsic piezoelectricity as a result of their non-centrosymmetric structure. As shown in Table 1, the in-plane piezoelectric stress coefficient, e_{11}, ranges from -1.87×10^{-10} Cm^{-1} for InTeCl to -1.31×10^{-10} Cm^{-1} for InTeI. Similarly, the in-plane piezoelectric strain coefficient, d_{11} , spans from -11.08 pmV^{-1} (InTeCl) to -6.75 pmV^{-1} (InTeI), indicating a strong electromechanical coupling effect. The out-of-plane coefficients, e_{31} and d_{31}, are smaller in magnitude but still present. The relaxed-ion piezoelectric coefficients e_{11} and d_{11} of pristine InTe monolayer are 0.69×10^{-10} Cm^{-1} and 1.18 pmV^{-1}, respectively.[53] For other members of the group-III monochalcogenides, MX (M = Ga, In and X = S, Se, Te) monolayers, the clamped-ion in-plane piezo coefficients e_{11} and d_{11} range from 5.17 to 5.39×10^{-10} Cm^{-1} and 8.29 to 13.26 pmV^{-1}, respectively.[53,54] These values comparable with those of the InTeX (X = Cl, Br, I) monolayers, confirming the good piezoelectricity of halogen functionalization. Furthermore, the systematic reduction in the absolute values of the piezoelectric coefficients from Cl to Br to I correlates directly with the decreasing electronegativity and increasing atomic radius of the halogen species.

This suggests that the highest piezoelectric performance is achieved with the lighter, most electronegative halogen (Cl), likely due to a greater induced asymmetry and charge transfer within the monolayer structure. These large piezoelectric coefficients make InTeX (X = Cl, Br, I) monolayers highly promising candidates for nanoscale applications such as piezoelectric sensors, transducers, actuators, active flexible electronics, and energy harvesting devices, particularly where high electromechanical coupling in a 2D material is required.

3.2 Electronic structure of InTeX (X = Cl, Br and I) monolayers

As a two-dimensional group III monochalcogenide with an intermediate indirect bandgap of 1.2–1.3 eV,[11,55] the InTe monolayer has shown considerable potential for nanoelectronic and photonic applications. Furthermore, its electronic properties can be effectively tuned through strain, external electric fields, or chemical doping, thereby broadening its application scope.[11] Therefore, it is essential to investigate the electronic properties of the halogenated InTeX (X = Cl, Br, I) monolayers, beginning with their band structures.

Fig. 5 displays the band structures obtained using both the conventional PBE functional (solid green lines) and the hybrid HSE06 functional (dashed pink lines). As expected, the HSE06 method predicts significantly wider bandgaps than PBE. The well-known bandgap underestimation in PBE arises from its approximate treatment of the exchange–correlation interaction, in which electrons partially interact with themselves. This self-interaction raises the energy levels of the valence bands and narrows the gap.[56,57] The discrepancy between PBE and HSE06 becomes more pronounced for heavier halogens, as reflected in Table 2, where the bandgap difference ranges from 0.76 to 0.85 eV and increases with halogen atomic mass (Cl → Br → I).

Compared to the pristine InTe monolayer with a reported bandgap of 1.94 eV,[12] the halogenated InTeCl and InTeBr monolayers exhibit wider bandgaps. However, with increasing halogen mass, the bandgap decreases; for instance, InTeI shows a slightly smaller gap than pristine InTe. This trend is consistent with observations in GaXY (X = S, Se; Y = F, Cl, Br, I) monolayers,[2] where lighter halogens (F, Cl) increase the bandgap, while heavier ones (Br, I) reduce it. A similar effect has been reported for GaTeCl, which exhibits an indirect bandgap of about 3.06 eV, substantially larger than the 1.4 eV gap of pristine GaTe.[58]

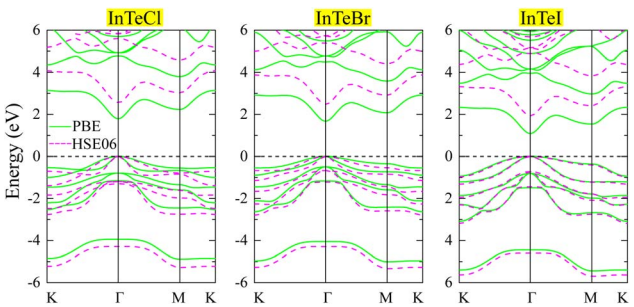

Fig. 5 Band structures of InTeX (X = Cl, Br, I) monolayers calculated using PBE (solid green line) and HSE06 (dash pink line) methods.

Table 2 Bandgap E_g (eV) calculated using PBE, HSE06, PBE + SOC, difference between the vacuum level $\Delta\Phi$ (eV), and work function on the of Te(x) side Φ_{Te} (Φ_X) (eV) InTeX monolayers (*X* represents Cl, Br and I)

	E_g^{PBE}	E_g^{HSE06}	$E_g^{PBE+SOC}$	$\Delta\Phi$	Φ_{Te}	Φ_X
InTeCl	1.79	1.53	2.55	2.01	5.45	7.46
InTeBr	1.67	1.43	2.48	1.46	5.34	6.80
InTeI	1.08	0.79	1.93	0.82	4.82	5.64

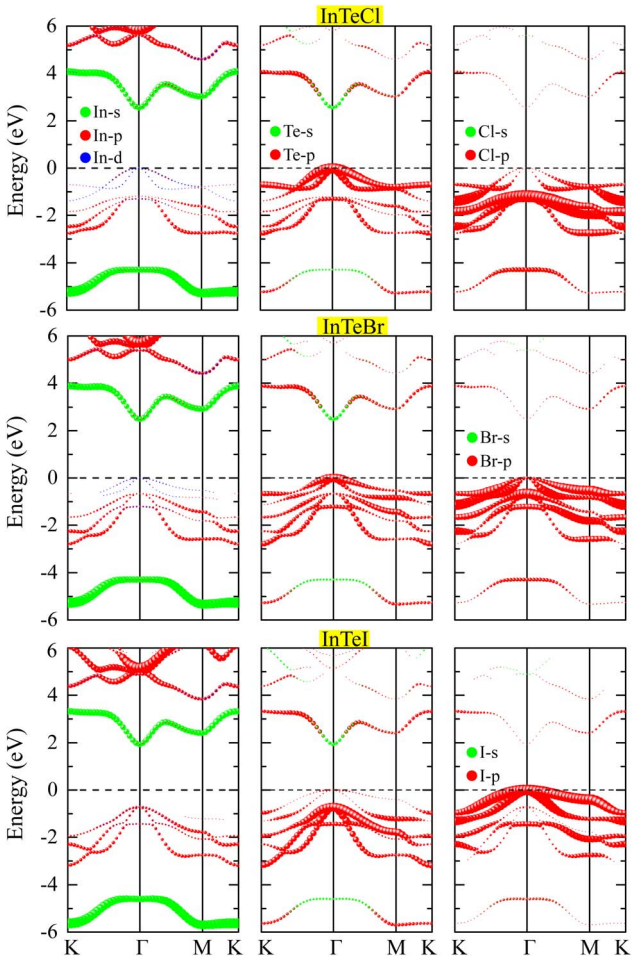

Fig. 6 Fat bands of InTeX (X = Cl, Br and I) monolayers.

Halogenation also alters the bandgap character of InTe. While the pristine InTe monolayer is an indirect-gap semiconductor,[12] the halogenated InTeX monolayers exhibit direct bandgaps. As shown in Fig. 5, both the valence band maximum (VBM) and conduction band minimum (CBM) are located at the Γ – point, confirming the direct bandgap nature of these systems. To further elucidate the mechanism by which halogenation modifies the bandgap character, the projected fat-band structures were calculated and are presented in Fig. 6.

The pristine InTe monolayer adopts a Te–In–In–Te stacking sequence, in which each In atom is fourfold coordinated, bonding to both Te and In atoms-forming a buckled layered geometry similar to InSe or GaTe monolayer.[13] This buckling hexagonal structure origins from the mixed sp^2–sp^3 hybridization, where the Te–In–In–Te configuration stabilizes through the mixing of Te–p and In–s/p/d orbitals.[13,15,59]

Before halogenation, the VBM is dominated by In–s and Te–p orbitals, reflecting strong p–s bonding localized within Te–In interactions, while the CBM primarily consists of Te–p and In–d orbitals that form antibonding states responsible for moderate band dispersion and interlayer covalency.[12,13] The two In layers are thus electronically coupled *via* s d hybridized orbitals, stabilizing the central In–In bonding framework. After halogenation, halogen atoms bond directly to the top In atoms, withdrawing charge density from the In–In bonds and weakening their coupling, thereby breaking the structural symmetry and yielding a single In layer sandwiched between Te and Cl, as shown in Fig. 1(b and c). The VBM consequently shifts to be dominated by Te–p and Cl/Br/I–p orbitals, as shown in Fig. 6, indicating that halogenation localizes the valence charge around the surface anions and diminishes the contribution of In-s orbitals. Meanwhile, the CBM becomes composed mainly of In–s, Te–s, and Te–p orbitals, signifying that conduction states now arise from out-of-plane hybridization between electronic states associated with In and Te rather than In–In coupling. This band structure evolution evidences the suppression of metallic In–In interactions and the emergence of polar covalent In–Cl, In–Br and In–I bonds, which elevate the conduction states and reshape the bonding topology.

Generally, this transformation is driven by orbital rehybridization. In pristine InTe, both In atoms engage in s–d hybridization along the vertical direction, forming strong metallic In–In bonds, whereas halogen adsorption introduces intense p–s interactions between halogen atoms and In atoms, leading to the formation of directional, ionic σ – bonds In–Cl, In–Br and In–I. As the In–s states become saturated through bonding with halogen atoms, the redundant In–In link collapses during relaxation, stabilizing the InTeX (X = Cl, Br and I) configuration. This process represents a transition from predominantly In–In metallic coupling to In–halogen polar covalent bonding, underpinning the observed structural and electronic reconstruction.

It can also be observed in Fig. 6 that, the Cl/Br/I–p orbitals are distributed deeper in the valence region, suggesting that these halogens primarily affect the electronic structure of InTeX (X = Cl, Br and I) monolayers by modifying the local potential and breaking inversion symmetry rather than contributing directly to states near the Fermi level. This orbital hybridization and structural asymmetry introduced by surface halogen adsorption are crucial factors possibly leading to the Rashba-type spin splitting. To explore this peculiarity, the band structures with spin–orbit coupling (SOC) effect were calculated for the three monolayers. It is evident in Fig. 7 that the three monolayers reveal Rashba effect with spin degeneracy at Γ – point, especially at the VBM. The Rashba characteristics are demonstrated in Fig. 7(d) and the values of these paramaters are summarized in Table 3.

As reported in Table 3, the splitting energy E_R is in the region of from 0.0079 to 0.0088 eV, while the momentum offset k_R is about from 0.0168 to 0.0195 $Å^{-1}$. These parameters yield the

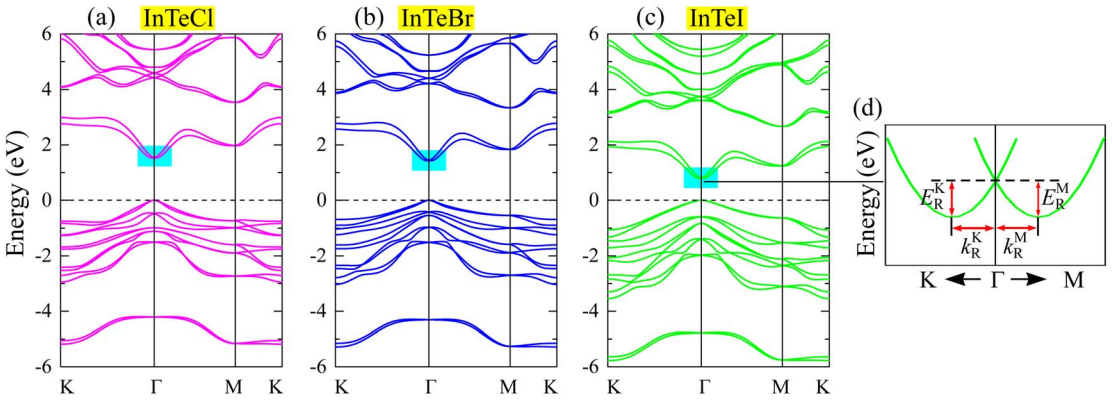

Fig. 7 Band structures including spin–orbit coupling for (a) InTeCl, (b) InTeBr, and (c) InTeI. Schematic illustration of Rashba-type spin splitting at the conduction band minimum (d).

Rashba coefficient $\alpha_R = 2E_R\, k_R^{-1}$ of from 0.8144 to 1.0414 eV Å, signifying a strong Rashba SOC in the InTeX (X = Cl, Br, I) monolayers. Monolayers with Rashba parameters in this range have been widely reported to enable diverse spintronic and optoelectronic applications, including short-channel spin-field-effect transistors (SFETs), Rashba thermoelectrics, spin–charge conversion, and gate-tunable spin-Hall devices. For instance, inverse-Janus monolayers with α_R of about 0.94 eV Å have been proposed for SFET and thermoelectric applications,[60] while Janus and group-III–V chalcogenide monolayers with α_R around 0.8–1.0 eV Å are suitable for spin–charge conversion and spin-Hall effects.[61] Moreover, strain- and twist-engineered Janus TMD bilayers such as MoSeTe/WSeTe, exhibiting tunable $\alpha_R \sim$ 1.0 eV Å, have been explored for flexible 2D spintronic, valleytronic, and opto-spintronics applications.[62] Therefore, InTeX monolayers with similar Rashba strengths have great potential as promising materials for next-generation spin-based and multifunctional nanodevices.

It is worth noting that the halogenated InTeX (X = Cl, Br, I) monolayers exhibit a significant anisotropic Rashba SOC, with the Rashba coefficient α_R consistently larger along the $\Gamma - M$ direction than along Γ − K. Specifically, α_R increases from 0.8969 eV Å (Γ − K) to 1.0414 eV Å (Γ − M) for InTeCl, from 0.8821 eV Å to 1.0178 eV Å for InTeBr, and from 0.8144 eV Å to 0.9524 eV Å for InTeI, while the corresponding Rashba energies E_R and momentum offsets k_R exhibit small difference between these directions. While halogen adsorption lowers the lattice symmetry from D_{3h} (centrosymmetric) to C_{3v}, enabling Rashba spin splitting by removing inversion symmetry, the observed directional anisotropy of α_R indicates a further reduction of symmetry below C_{3v}. Across the halogen series, the absolute magnitude of α_R decreases slightly from Cl to I, consistent with a reduced out-of-plane dipole moment as halogen electronegativity decreases. This anisotropic Rashba behavior is analogous to that observed in Janus transition-metal dichalcogenides (TMDs) such as MoSSe and WSeTe, and in Pt-based Janus dichalcogenides, where symmetry lowering yields unequal α_R values along Γ − K and Γ − M.[63,64]

Monolayers possessing such anisotropic Rashba SOC provide direction-selective control of spin dynamics, as the differing α_R values along crystallographic axes allow orientation-dependent spin precession and spin-filtering in spin-field-effect transistors (SFETs) and logic architectures.[61,65,66] The anisotropy further enhances spin–charge interconversion, with efficiency and spin polarization tunable by transport direction, strain, or gate bias.[67–69] Consequently, halogenated InTeX monolayers emerge as promising candidates for orientation-programmable spintronic, optospintronic, and valleytronic devices, offering reconfigurable, low-power platforms for future two-dimensional spin logic and quantum information technologies. It is noted that epitaxial strain is expected to effectively tune the electronic and spintronic properties of InTeX (X = Cl, Br, and I) monolayers by modifying the band dispersion and Rashba spin splitting. While a detailed strain-dependent analysis is beyond the scope of this work, the present results provide a solid foundation for future strain-engineering studies and practical device optimization.

The charge distribution of Janus halogenated InTeX (X = Cl, Br, I) monolayers can be further characterized by analyzing their work functions and Bader charge profiles. As shown in Fig. 8(a), the electrostatic potential profiles reveal a pronounced potential drop across the layer, with $\Delta\Phi$ ranging from 0.82 to 2.01 eV as summerized in Table 2), indicating a significant internal electric field directed from the Te sublayer toward the halogen atoms. This internal field arises from charge transfer between In and X atoms, as confirmed by the Bader charge values listed in Table 3, which shows that the halogen atoms gain electrons while indium loses charge, as shown in Fig. 8(b). Such charge redistribution creates a net dipole moment that decreases progressively from Cl to I, consistent with the reduction in halogen electronegativity. The corresponding work function difference between the top and bottom surfaces further reflects

Table 3 Electronic structure of InTeX (X = Cl, Br and I) monolayers: splitting energy E_R (eV),momentum offset k_R (Å^{-1})and Rashba parameter α_R (eV Å)

	E_R^K	E_R^M	k_R^K	k_R^M	α_R^K	α_R^M
InTeCl	0.0087	0.0088	0.0194	0.0169	0.8969	1.0414
InTeBr	0.0086	0.0086	0.0195	0.0169	0.8821	1.0178
InTeI	0.0079	0.008	0.0194	0.0168	0.8144	0.9524

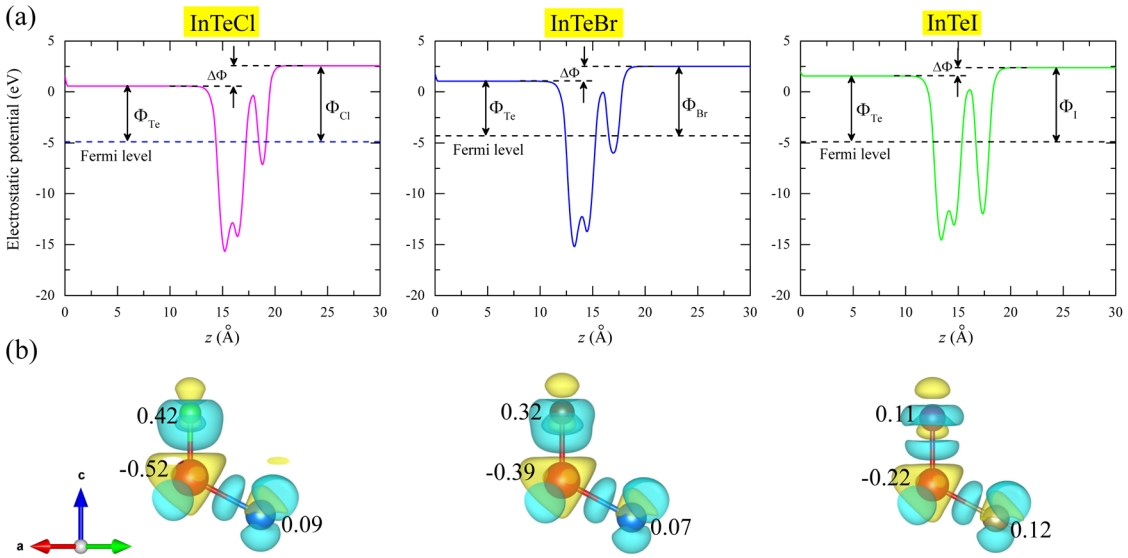

Fig. 8 (a) Electrostatic potentials and (b) electron density differences of InTeX (X = Cl, Br, and I) monolayers. The yellow regions in (b) denote electron depletion with negative Bader charge, while the blue regions indicate electron accumulation with positive Bader charge.

this polarity, with InTeCl exhibiting the largest potential asymmetry and hence the strongest built-in field. According to the Helmholtz relation, this field induces substantial spin splitting through Rashba SOC,[70,71] explaining the larger α_R values observed in InTeCl compared with InTeBr and InTeI.

3.3 Transport properties of InTeX (X = Cl, Br, and I) monolayers

In two-dimensional materials, charge transport is mainly governed by phonon-induced scattering due to reduced dimensionality and weakened dielectric screening. In the following, we present the phonon-limited carrier mobility calculated using the AMSET package,[31] which enables a quantitative evaluation of the contributions from different phonon scattering mechanisms within the Boltzmann transport framework. All relevant input parameters are derived from first-principles calculations. The four scattering mechanisms included in the transport calculations are acoustic-deformation-potential scattering (ADP), ionized-impurity scattering (IMP), piezoelectric scattering (PIE) and polar-optical-phonon scattering (POP). Each mechanism contributes a separate resistance to carrier motion, and Matthiessen's rule assumes these processes act independently, so their scattering rates simply add to determine the overall mobility limit. The total mobiltiy μ_{TOT} can be calculated as:[32,72,73]

$$\frac{1}{\mu_{TOT}} = \frac{1}{\mu_{ADP}} + \frac{1}{\mu_{IMP}} + \frac{1}{\mu_{PIE}} + \frac{1}{\mu_{POP}} \quad (3)$$

Fig. 9 and 10 illustrate the temperature dependence of the carrier mobility at different carrier concentration in the studied InTeX monolayers, presenting both the carrier mobilities limited by individual phonon scattering mechanisms and the resulting total carrier mobility. In general, carrier mobility depends on the carrier concentration. Here, we choose two carrier concentration values n_c of 1×10^{16} and 1×10^{20} cm^{-3}, which represent the low- and high-carrier-concentration regimes, respectively. Fig. 9(a) shows that POP and PIE scattering play major roles in determining the total electron mobility in the proposed InTeX (X = Cl, Br, I) monolayers. In the low carrier concentration regime of 1×10^{16} cm^{-3}, the contributions of POP and PIE scattering to the electron mobility are nearly comparable in the InTeCl monolayer, whereas a pronounced difference is observed in the other two structures. Specifically, POP scattering is the dominant mechanism limiting the total electron mobility in the InTeBr monolayer, while the total electron mobility in the InTeI monolayer is primarily limited by PIE scattering.

In the high carrier concentration regime, namely $n_c = 1 \times 10^{20}$ cm^{-3}, POP scattering emerges as the dominant mechanism limiting the total electron mobility in the InTeCl and InTeBr monolayers as depicted in Fig. 10(a). This behavior can be attributed to the enhanced electron–phonon coupling with polar optical modes at elevated carrier densities, where increased screening and occupation effects significantly amplify POP scattering rates. In contrast, in the InTeI monolayer, the total electron mobility is primarily governed by PIE scattering, indicating that long-wavelength acoustic phonons associated with lattice polarization play a more prominent role in carrier transport in this structure. In contrast to the electron case, the total hole mobility is predominantly governed by ADP scattering in both the low- and high-carrier concentration regimes, particularly in the high temperature region. This indicates that hole transport is mainly limited by interactions with long-wavelength acoustic phonons, whose scattering strength is relatively insensitive to carrier density. The different temperature dependences of the hole mobility observed in Fig. 9 and 10 arise from the distinct carrier concentration regimes considered. At high carrier concentration, enhanced screening and carrier–carrier interactions reduce the effective scattering

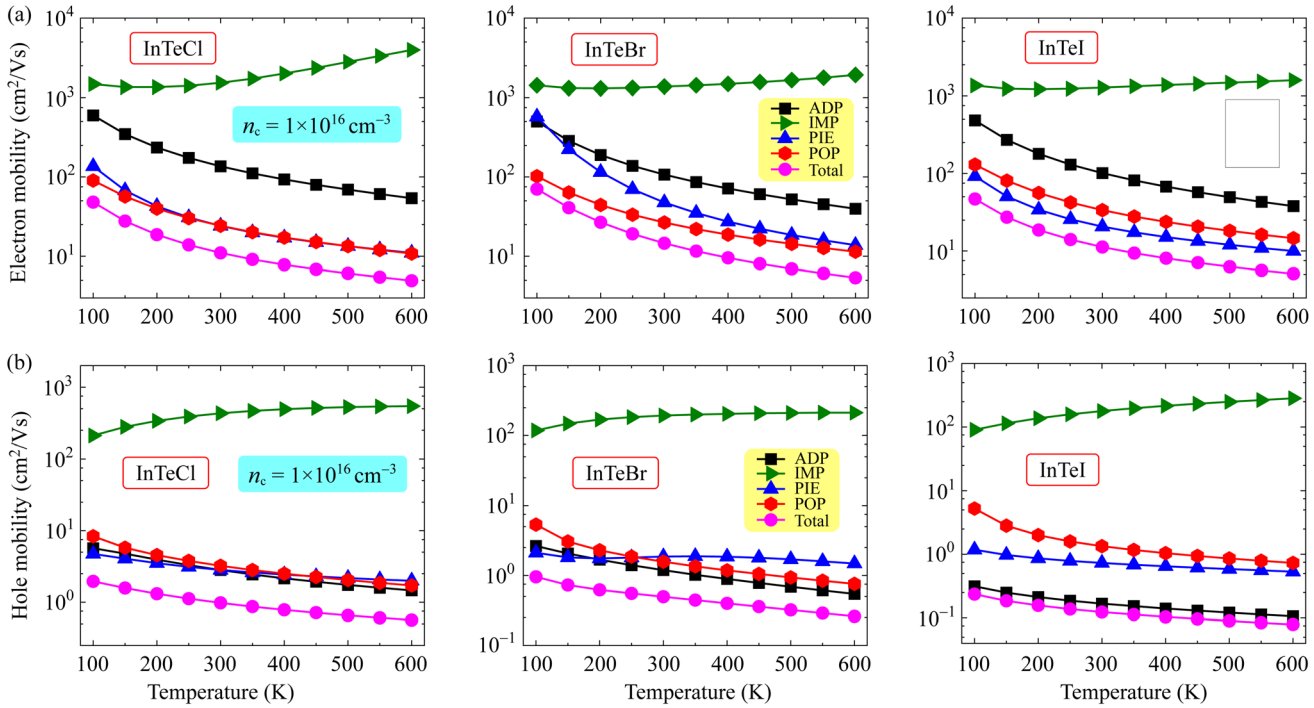

Fig. 9 Temperature-dependent phonon-limited and total electron (a) and hole (b) mobilities of InTeX (X = Cl, Br, and I) monolayers at a low carrier concentration of 1×10^{16} cm^{-3}.

strength. This screening effect partially compensates for the increased phonon scattering at elevated temperatures, leading to a modified mobility-temperature dependence.

Presenting carrier mobility at room temperature is particularly important because it directly reflects the practical transport performance of materials under realistic operating conditions. Since most electronic and optoelectronic devices function near room temperature, carrier mobility evaluated at this temperature provides a meaningful benchmark for assessing device feasibility and for comparison with

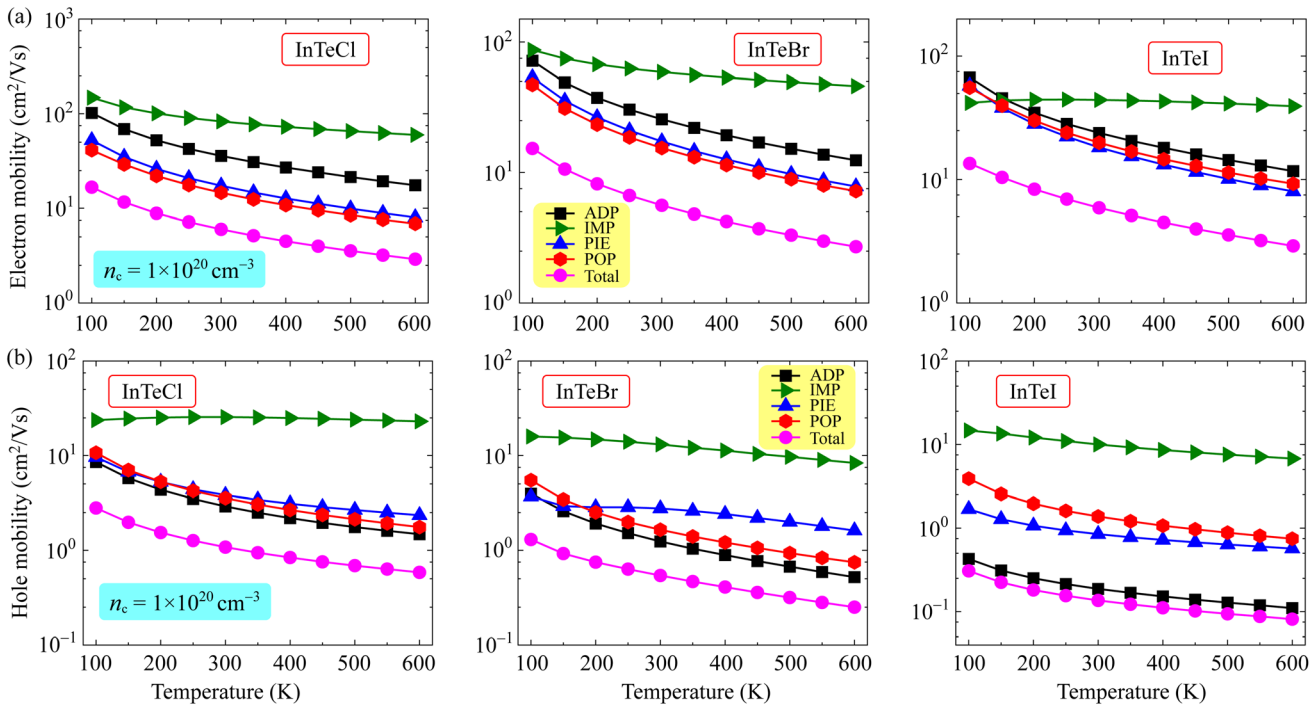

Fig. 10 Temperature-dependent phonon-limited and total electron (a) and hole (b) mobilities of InTeX (X = Cl, Br, and I) monolayers at a high carrier concentration of 1×10^{20} cm^{-3}.

Table 4 Room-temperature phonon-limited and total carrier mobilities μ ($cm^2 V^{-1} s^{-1}$) of InTeX (X = Cl, Br, and I) monolayers at different carrier concentrations n_c (cm^{-3})

Carrier type	Compound	n_c	μ_{ADP}	μ_{IMP}	μ_{PIE}	μ_{POP}	μ_{total}
Electron	InTeCl	1×10^{16}	1.36×10^2	1.53×10^3	24.10	24.20	11.01
	InTeBr		1.07×10^2	1.37×10^3	47.60	26.60	14.56
	InTeI		1.01×10^2	1.27×10^3	20.60	33.60	11.24
	InTeCl	1×10^{20}	35.80	83.00	17.30	14.60	6.01
	InTeBr		25.60	58.90	17.30	15.40	5.59
	InTeI		23.90	44.30	18.20	19.90	5.90
Hole	InTeCl	1×10^{16}	2.81	4.32×10^2	2.82	3.22	0.98
	InTeBr		1.19	1.93×10^2	1.86	1.57	0.50
	InTeI		0.18	1.78×10^2	0.73	1.34	0.12
	InTeCl	1×10^{20}	2.91	25.50	3.82	3.55	1.08
	InTeBr		1.24	13.10	2.77	1.65	0.54
	InTeI		0.19	10.00	0.85	1.38	0.14

experimental measurements. Moreover, room-temperature mobility inherently captures the combined effects of various scattering mechanisms, especially phonon scattering, which dominates charge transport in this regime. The calculated carrier mobilities at room temperature are summarized in Table 4. At low carrier concentrations, namely $n_c = 1 \times 10^{16}$ cm^{-3}, the electron mobility ranges from 11.01 to 14.56 $cm^2 V^{-1} s^{-1}$, but it decreases significantly to about 6 $cm^2 V^{-1} s^{-1}$ as the carrier concentration increases. This reduction in electron mobility at higher carrier concentrations can be attributed to enhanced carrier–carrier and carrier–phonon scattering, as well as increased screening effects that modify the electron–phonon coupling strength. In contrast, the hole mobility at room temperature remains relatively low for both low and high carrier concentration regimes. This behavior suggests that hole transport is intrinsically limited, likely due to the heavier effective mass and stronger coupling to lattice vibrations, making it less sensitive to changes in carrier concentration compared to electron transport. The room-temperature carrier mobilities of halogenated InTeX (X = Cl, Br, and I) monolayers obtained in this work are much lower than the exceptionally high electron mobility previously reported for the InTeI monolayer using the deformation-potential (DP) approach (12 137.80 $cm^2 V^{-1} s^{-1}$).[16] This discrepancy mainly arises from the simplified nature of the DP method, which considers only acoustic-phonon scattering and therefore tends to significantly overestimate carrier mobility. In contrast, more rigorous Boltzmann transport calculations and experimental measurements for representative 2D materials, such as MoS_2 and phosphorene, consistently yield much lower mobilities than those predicted by the DP model.[74–76] Furthermore, the electron and hole mobilities of pristine InTe monolayers obtained with full scattering effects included are 18 and 0.2 $cm^2 V^{-1} s^{-1}$, respectively, which are comparable to those of the InTeX systems,[21] thereby supporting the reliability of the carrier mobility calculations presented in this work.

4 Conclusion

In this work, first-principles calculations were employed to elucidate the structural reconstruction, stability, electronic properties, and transport characteristics of halogenated InTeX (X = Cl, Br, and I) monolayers derived from pristine InTe. The moderate electronegativities of Cl, Br, and I enable the formation of energetically, mechanically, and dynamically stable Te–In–X three-sublayer configurations, where halogen adsorption suppresses the In–In bond and transforms the original Te–In–In–Te stacking into a polar, non-centrosymmetric lattice. This reconstruction converts pristine InTe into a direct-gap semiconductor with tunable bandgaps decreasing from Cl to I, and simultaneously generates strong, anisotropic Rashba spin splitting driven by inversion-symmetry breaking and internal electric dipoles. Importantly, the charge carrier mobilities were calculated by explicitly accounting for phonon and impurity scattering, resulting in values that are more consistent with experimental measurements and considerably lower than the overestimated mobilities reported in previous studies using only the deformation-potential approach. Such accurate mobility assessments are essential for evaluating practical device performance, especially in flexible electronics, spin–orbit devices, and photocatalytic systems where transport limitations strongly influence their efficiency. In addition, the distinctive three-peak Raman fingerprints, dominated by a characteristic lower A_1 mode, provide a clear experimental marker for phase identification. The halogenated InTeX (X = Cl, Br, and I) monolayers are also observed to possess good piezoelectricity. Altogether, the stable, polar, and electronically tunable InTeX monolayers constitute a new branch of 2D III–VI materials, offering promising opportunities for flexible nanoelectronics, spintronic architectures, and future exploration of halogen-induced reconstruction across group-III monochalcogenides.

Conflicts of interest

The authors have no conflicts of interest to disclose.

Data availability

All data that support the findings of this study are included within the article.

References

1 C. Ren, S. Wang, H. Tian, Y. Luo, J. Yu, Y. Xu and M. Sun, *Sci. Rep.*, 2019, **9**, 13289.
2 R. Guo, R. Zhao, Y. Ge, Y. Liu and W. Wan, *Appl. Phys. Lett.*, 2023, **123**, 063102.
3 Y. Cai, G. Zhang and Y.-W. Zhang, *J. Phys. Chem. C*, 2017, **121**, 10182–10193.
4 M. Yagmurcukardes, *Phys. Rev. B*, 2016, **100**, 024108.
5 Z.-Y. Chen, M. Xiong, Z.-Y. Zeng, X.-R. Chen and Q.-F. Chen, *Solid State Commun.*, 2021, **326**, 114163.
6 M. I. Zappia, G. Bianca, S. Bellani, N. Curreli, Z. e. Sofer, M. Serri, L. Najafi, M. Piccinni, R. Oropesa-Nuñez, P. Marvan, *et al.*, *J. Phys. Chem. C*, 2021, **125**, 11857–11866.
7 S. Lei, L. Ge, S. Najmaei, A. George, R. Kappera, J. Lou, M. Chhowalla, H. Yamaguchi, G. Gupta, R. Vajtai, *et al.*, *ACS Nano*, 2014, **8**, 1263–1272.
8 S. Zhou, C.-C. Liu, J. Zhao and Y. Yao, *npj Quantum Mater.*, 2018, **3**, 16.
9 T. M. Duyen Huynh, T. D. Hien Nguyen and M.-F. Lin, *ACS Omega*, 2022, **7**, 34868–34876.
10 S. Wang, H. Tian, Y. Luo, J. Yu, C. Ren, C. Sun, Y. Xu and M. Sun, *Appl. Surf. Sci.*, 2019, **481**, 1549–1553.
11 T.-N. Do, V. T. Vi, N. T. Binh, N. N. Hieu and N. V. Hieu, *Superlattices Microstruct.*, 2021, **151**, 106816.
12 Y. Liao, H. Liu, G. Yuan, Z. Huang and X. Qi, *Cryst. Res. Technol.*, 2020, **55**, 2000102.
13 S. Demirci, N. Avazlı, E. Durgun and S. Cahangirov, *Phys. Rev. B*, 2017, **95**, 115409.
14 M. Chen, R. Xue and P. Wu, *J. Phys. Chem. C*, 2024, **128**, 13568–13576.
15 K. Li, X. Xian, J. Wang and N. Yu, *Appl. Surf. Sci.*, 2019, **471**, 18–22.
16 S. Jiang, J. Li, W. Chen, H. Yin, G.-P. Zheng and Y. Wang, *Nanoscale*, 2020, **12**, 5888–5897.
17 S. J. Khengar, H. R. Mahida, H. P. Patel and P. B. Thakor, *ACS Appl. Nano Mater.*, 2024, **7**, 17648–17658.
18 H. Sun, S.-S. Li, W.-x. Ji and C.-W. Zhang, *Phys. Rev. B*, 2022, **105**, 195112.
19 B. Wu, Y.-l. Song, W.-x. Ji, P.-j. Wang, S.-f. Zhang and C.-w. Zhang, *Phys. Rev. B*, 2023, **107**, 214419.
20 S.-j. Zhang, C.-w. Zhang, S.-f. Zhang, W.-x. Ji, P. Li, P.-j. Wang, S.-s. Li and S.-s. Yan, *Phys. Rev. B*, 2017, **96**, 205433.
21 L. Cheng, C. Zhang and Y. Liu, *Comput. Mater. Sci.*, 2021, **194**, 110468.
22 G. Kresse and J. Furthmüller, *Phys. Rev. B: Condens. Matter Mater. Phys.*, 1996, **54**, 11169–11186.
23 G. Kresse and J. Furthmüller, *Comput. Mater. Sci.*, 1996, **6**, 15–50.
24 J. P. Perdew, K. Burke and M. Ernzerhof, *Phys. Rev. Lett.*, 1996, **77**, 3865.
25 D. D. Vo, T. V. Vu, A. Kartamyshev, T. H. Ho and N. N. Hieu, *Nanoscale Adv.*, 2024, **6**, 6019–6028.
26 S. Grimme, J. Antony, S. Ehrlich and H. Krieg, *J. Chem. Phys.*, 2010, **132**, 154104.
27 J. Heyd, G. E. Scuseria and M. Ernzerhof, *J. Chem. Phys.*, 2003, **118**, 8207.
28 H. J. Monkhorst and J. D. Pack, *Phys. Rev. B: Condens. Matter Mater. Phys.*, 1976, **13**, 5188.
29 A. Togo, L. Chaput, T. Tadano and I. Tanaka, *J. Phys.: Condens. Matter*, 2023, **35**, 353001.
30 A. Togo, *J. Phys. Soc. Jpn.*, 2023, **92**, 012001.
31 A. M. Ganose, J. Park, A. Faghaninia, R. Woods-Robinson, K. A. Persson and A. Jain, *Nat. Commun.*, 2021, **12**, 2222.
32 L. Cheng and Y. Liu, *J. Am. Chem. Soc.*, 2018, **140**, 17895–17900.
33 A. Matetskiy, V. Mararov, A. Mihalyuk, N. Denisov, S. Eremeev, A. Zotov and A. Saranin, *Phys. Rev. B*, 2022, **106**, 165301.
34 V. Zólyomi, N. Drummond and V. Fal'Ko, *Phys. Rev. B*, 2014, **89**, 205416.
35 K. H. Yeoh, T. L. Yoon, D. Ong, T. Lim, *et al.*, *IOP Conf. Ser.:Mater. Sci. Eng.*, 2019, 012001.
36 M. R. Molas, A. V. Tyurnina, V. Zólyomi, A. K. Ott, D. J. Terry, M. J. Hamer, C. Yelgel, A. Babiński, A. G. Nasibulin, A. C. Ferrari, *et al.*, *Faraday Discuss.*, 2021, **227**, 163–170.
37 X. Zeng, Y. Chen, Y. Jiang, L. Sui, A. Chen and M. Jin, *J. Appl. Phys.*, 2024, **136**, 065101.
38 A. K. Katiyar, A. T. Hoang, D. Xu, J. Hong, B. J. Kim, S. Ji and J.-H. Ahn, *Chem. Rev.*, 2023, **124**, 318–419.
39 M. Lanza, Q. Smets, C. Huyghebaert and L.-J. Li, *Nat. Commun.*, 2020, **11**, 5689.
40 N. J. Singh, I. Basumatary, C. S. R. Kolli and P. Sahatiya, *Chem. Commun.*, 2025, **61**, 11158–11186.
41 D. D. Vo, T. V. Vu, A. Kartamyshev, T. H. Ho and K.-M. Bui, *RSC Adv.*, 2025, **15**, 24236–24246.
42 F. Mouhat and F.-X. Coudert, *Phys. Rev. B: Condens. Matter Mater. Phys.*, 2014, **90**, 224104.
43 G. Sahoo and A. Biswal, *Phys. B*, 2025, **697**, 416742.
44 G. Qin, Z. Qin, W.-Z. Fang, L.-C. Zhang, S.-Y. Yue, Q.-B. Yan, M. Hu and G. Su, *Nanoscale*, 2016, **8**, 11306–11319.
45 L. Webster and J.-A. Yan, *Phys. Rev. B*, 2018, **98**, 144411.
46 K. Liu, Q. Yan, M. Chen, W. Fan, Y. Sun, J. Suh, D. Fu, S. Lee, J. Zhou, S. Tongay, *et al.*, *Nano Lett.*, 2014, **14**, 5097–5103.
47 M. Yagmurcukardes, R. T. Senger, F. M. Peeters and H. Sahin, *Phys. Rev. B*, 2016, **94**, 245407.
48 L. Wang, A. Kutana, X. Zou and B. I. Yakobson, *Nanoscale*, 2015, **7**, 9746–9751.
49 N. T. Hung, A. R. Nugraha and R. Saito, *J. Phys. D: Appl. Phys.*, 2018, **51**, 075306.
50 J. Tang, Q. Wang, J. Tian, X. Li, N. Li, Y. Peng, X. Li, Y. Zhao, C. He, S. Wu, *et al.*, *Nat. Commun.*, 2023, **14**, 3633.
51 A. Lipatov, H. Lu, M. Alhabeb, B. Anasori, A. Gruverman, Y. Gogotsi and A. Sinitskii, *Adv. Sci.*, 2018, **4**, eaat0491.
52 N. R. Glavin, C. Muratore and M. Snure, *Oxford Open Mater. Sci.*, 2021, **1**, itaa002.
53 Y. Guo, S. Zhou, Y. Bai and J. Zhao, *Appl. Phys. Lett.*, 2017, **110**, 163102.
54 W. Li and J. Li, *Nano Res.*, 2015, **8**, 3796–3802.
55 A. Šolajić and J. Pešić, *Sci. Rep.*, 2024, **14**, 1081.
56 P. Mori-Sánchez, A. J. Cohen and W. Yang, *Phys. Rev. Lett.*, 2008, **100**, 146401.

57 P. Borlido, J. Schmidt, A. W. Huran, F. Tran, M. A. Marques and S. Botti, *npj Comput. Mater.*, 2020, **6**, 96.
58 W. Zhou, S. Guo, S. Zhang, Z. Zhu, X. Song, T. Niu, K. Zhang, X. Liu, Y. Zou and H. Zeng, *Nanoscale*, 2018, **10**, 3350–3355.
59 X. Yao and X. Zhang, *ACS Omega*, 2021, **6**, 13426–13432.
60 Q. Tian, P. Li, J. Wei, Z. Xing, G. Qin and Z. Qin, *Phys. Rev. B*, 2023, **108**, 115130.
61 S. Babaee Touski and N. Ghobadi, *Phys. Rev. B*, 2021, **103**, 165404.
62 A. Rezavand and N. Ghobadi, *J. Magn. Magn. Mater.*, 2022, **544**, 168721.
63 P. A. L. Sino, L.-Y. Feng, R. A. B. Villaos, H. N. Cruzado, Z.-Q. Huang, C.-H. Hsu and F.-C. Chuang, *Nanoscale Adv.*, 2021, **3**, 6608–6616.
64 Q. Zhang and U. Schwingenschlögl, *Phys. Rev. B*, 2018, **97**, 155415.
65 T. Hu, F. Jia, G. Zhao, J. Wu, A. Stroppa and W. Ren, *Phy. Rev. B*, 2018, **97**, 235404.
66 S. Datta and B. Das, *Appl. Phys. Lett.*, 1990, **56**, 665–667.
67 T. S. Ghiasi, A. A. Kaverzin, P. J. Blah and B. J. Van Wees, *Nano Lett.*, 2019, **19**, 5959–5966.
68 A. Johansson, J. Henk and I. Mertig, *Phys. Rev. B*, 2016, **93**, 195440.
69 S. Leiva-Montecinos, J. Henk, I. Mertig and A. Johansson, *Phys. Rev. Res.*, 2023, **5**, 043294.
70 S. R. Park, C. H. Kim, J. Yu, J. H. Han and C. Kim, *Phys. Rev. Lett.*, 2011, **107**, 156803.
71 J. Hong, J.-W. Rhim, C. Kim, S. Ryong Park and J. Hoon Shim, *Sci. Rep.*, 2015, **5**, 13488.
72 T. V. Vu, L. V. Hung, L. T. Phuong, H. V. Phuc, C. V. Nguyen, A. I. Kartamyshev and N. N. Hieu, *J. Phys. Chem. C*, 2025, **129**, 20003–20014.
73 T. V. Vu, L. V. Hung, C. V. Nguyen, N. T. Hiep, K.-M. Bui, A. Kartamyshev and N. N. Hieu, *Appl. Phys. Lett.*, 2025, **127**, 081601.
74 J. Qiao, X. Kong, Z.-X. Hu, F. Yang and W. Ji, *Nat. Commun.*, 2014, **5**, 4475.
75 K. Kaasbjerg, K. S. Thygesen and K. W. Jacobsen, *Phys. Rev. B: Condens. Matter Mater. Phys.*, 2012, **85**, 115317.
76 B. Liao, J. Zhou, B. Qiu, M. S. Dresselhaus and G. Chen, *Phys. Rev. B*, 2015, **91**, 235419.